

New evidence and impact of electron transport non-linearities based on new perturbative inter-modulation analysis

メタデータ	<p>言語: eng</p> <p>出版者:</p> <p>公開日: 2021-12-28</p> <p>キーワード (Ja):</p> <p>キーワード (En):</p> <p>作成者: BERKEL, Matthijs van, Kobayashi, Tatsuya, IGAMI, Hiroe, VANDERSTEEN, Gerd, HOGWEIJ, G.M.D., TANAKA, Kenji, TAMURA, Naoki, ZWART, H.J., KUBO, Shin, ITO, Satoshi, TSUCHIYA, Hayato, DE BAAR, Marco Richard, LHD, Experiment Group</p> <p>メールアドレス:</p> <p>所属:</p>
URL	http://hdl.handle.net/10655/00012862

This work is licensed under a Creative Commons Attribution-NonCommercial-ShareAlike 3.0 International License.



New evidence and impact of electron transport non-linearities based on new perturbative inter-modulation analysis

M. van Berkel^{1,2,3}, T. Kobayashi⁴, H. Igami⁴,
G. Vandersteen¹, G.M.D. Hogeweyj², K. Tanaka⁴,
N. Tamura⁴, H.J. Zwart^{5,6}, S. Kubo⁴, S. Ito⁴, H. Tsuchiya⁴,
M.R. de Baar^{2,7}, and the LHD Experiment Group

¹Vrije Universiteit Brussel (VUB), Dept. of Fundamental Electricity and Instrumentation, Pleinlaan 2, 1050 Brussels, Belgium

²DIFFER - Dutch Institute for Fundamental Energy Research, PO Box 6336, 5600HH Eindhoven, The Netherlands

³Fellow of the Japan Society for the Promotion of Science (JSPS)

⁴National Institute for Fusion Science, 322-6 Oroshi-cho, Toki-city, Gifu, 509-5292, Japan

⁵Eindhoven University of Technology, Dept. of Mechanical Engineering, Dynamics and Control Group, PO Box 513, 5600MB Eindhoven, The Netherlands

⁶University of Twente, Dept. of Applied Mathematics, PO Box 217, 7500AE, Enschede, The Netherlands

⁷Eindhoven University of Technology, Dept. of Mechanical Engineering, Control Systems Technology Group, PO Box 513, 5600MB Eindhoven, The Netherlands

Abstract. A new methodology to analyze non-linear components in perturbative transport experiments is introduced. The methodology has been experimentally validated in the Large Helical Device (LHD) for the electron heat transport channel. Electron cyclotron resonance heating (ECRH) with different modulation frequencies by two gyrotrons has been used to directly quantify the amplitude of the non-linear component at the inter-modulation frequencies. The measurements show significant quadratic non-linear contributions and also the absence of cubic and higher order components. The non-linear component is analyzed using Volterra series, which is the non-linear generalization of transfer functions. This allows us to study the radial distribution of the non-linearity of the plasma and to reconstruct linear profiles in the case in which the measurements were not distorted by non-linearities. The reconstructed linear profiles are significantly different from the measured profiles showing the significant impact that the non-linearity can have.

1. Introduction

Plasma turbulence or anomalous transport deteriorates energy confinement in contemporary magnetically confined fusion devices. Therefore, seeking to improve energy confinement, a number of methodologies have been developed to analyze transport. These methodologies focus either on the micro-scale level [1] or on the global consequences of turbulence, e.g., temperature (gradient) and transport coefficients such as diffusion [2]. These quantities are generally analyzed in 1D as a function of the dimensionless normalized minor radius ρ , which is permissible due to the device geometry, magnetic field configuration, and relevant time scales of transport [3]. This radial transport is then analyzed in steady-state [4] or in the transient phase, often using a perturbation [2, 3, 5, 6].

In perturbative experiments a source or multiple sources are modulated and the resulting perturbations are studied. The reason is that this allows the separation of different transport quantities. Consequently, these studies allow a deeper understanding of the underlying physics, which is often non-linear.

Different modulated sources can be used to perturb various transport channels, such as: the electron heat transport by electron cyclotron resonance heating (ECRH) [7, 8, 9], repetitive pellet injection [10], or using a minority heating scheme [11]; particle transport using modulated gas-puffing with helium [12, 13]; momentum transport using modulated neutral beam injection (NBI) to modulate the torque [14, 15, 16]; the ion heat transport using ion cyclotron resonance heating [17, 18]; and the analysis of impurity transport using, for instance, laser blow-off of boron and carbon materials [19]. This list is far from exhaustive. For a more complete overview of such experiments and its history the reader is referred to [2, 3, 20].

In this paper, periodic transient measurements are analyzed in the frequency domain where the change of amplitude and phase (delay) of the spatial propagation of the perturbation are crucial to interpret the effect of turbulence on overall transport [17, 21]. Currently, the proper interpretation and results derived from the amplitude and phase profiles require the validity of the small perturbation theory (linearity). Hence, we introduce frequency inter-modulation [22, 23, 24] in combination with a newly developed experimental analysis method based on Volterra series [25]. Not

only can the linearity property in a single experiment be validated, but more importantly the spatially distributed non-linear transport properties can be studied. The linear profiles can be reconstructed by removing the non-linear contributions resulting in a significantly different corrected profile compared to the measured profiles.

We focus on perturbative electron heat transport because the electron transport can be considered decoupled from the other transport channels when using modulated ECRH and a low-density (low-collisionality) plasma. There are several non-linearities proposed in the literature. The most common are dependencies of the diffusivity on the temperature or the temperature gradient, where the latter is considered to be rather weak in LHD [2, 26]. In addition, other important sources of non-linearity and non-locality are streamers [27], avalanches [28], and MHD mode coupling [29]. Current literature related to LHD points towards a power dependence of transport via the turbulence level [30], which has also been extensively studied at W7-AS [31, 32, 33]. These and other non-linear transport properties have been analyzed using perturbations (often via the heat pulse diffusivity χ_{HP}) at different operating points and comparing them to each other and to steady-state results (power balance diffusivity χ_{PB}) [2, 34]. Alternatively, model codes based on physics are used to fit parameters of the non-linear models, e.g., [20, 35]. The problem with such an approach is that although the existence of a non-linearity can be proven, the interpretation of the non-linearity depends on the used transport model. An example is the heat diffusivity χ_{HP} . It can be estimated from measurements in which the amplitude of the perturbation is sufficiently small such that the physics can be described by a linearized transport model. If χ_{HP} changes with a change in the operating point, it is a clear sign of non-linearity. However, if the perturbation is not sufficiently small the presumed perturbative "linear" measurements from which χ_{HP} is estimated is distorted by a non-linear component. This results in an incorrect estimate of χ_{HP} . Consequently, describing the non-linearity with linear models at different operating points only captures part of the non-linear behaviour, and in the case in which the linear models are estimated from measurements distorted by non-linear components, they neither describe the linearized physics nor capture the full non-linearities.

In this paper, we apply a measurement driven approach in which the amplitude of the non-linearity can be directly detected at the inter-modulation frequencies. The advantage of this approach is that the non-linearity becomes separable from the choice of the specific transport model. In addition, this method allows confirming the validity of the assumption of linearity in the particular experiment, which is crucial in the linear interpretation of transport experiments. Volterra series are used to reconstruct the linear and amplitude profiles distorted due to the non-zero average of the perturbation. It is also possible to calculate the local non-linear contribution with some additional assumptions.

The method is based upon an induced perturbation with two different frequencies, f_1 and f_2 . As a result of non-linear transport properties, these sum and difference harmonics should become non-zero components. Hence, their amplitude is a measure of the non-linearity. This analysis has some similarity to the bi-coherence analysis [36], but with the important difference that the plasma is actively perturbed. In principle, it is possible to use one source term to create such perturbations. However, given the constraints on the modulation, it is often not possible to produce such a perturbation. This is also true in ECRH experiments. Therefore, alternatively, two sources with block modulations are used.

The inter-modulation method or two-tone method has been a common method for studying non-linearities in electric circuits for a long time [24, 37]. To our knowledge, this method has been used only once with regard to transport studies in fusion plasmas [23]. The conclusions of that experiment on W7-AS were that no inter-modulations were detected and that extreme sensitivities of the electron-cyclotron-emission (ECE)-system are necessary to detect such inter-modulations [23]. One of the reasons that make it difficult to detect non-linearities at the inter-modulation frequencies is that the chosen modulation frequencies for f_1 and f_2 resulted in rather large inter-modulation frequencies 158 Hz and 342 Hz. Consequently, the diffusive transport is dominant, which suppresses the amplitude of the sum and difference contributions making them more difficult to detect compared to lower modulation frequencies. Hence, in the experiment presented here we use significantly lower inter-modulation frequencies. As a result the thermal transport component of the propagation is less dominant. However, these frequency components are subject to low frequency perturbations such as the natural response due to the change from one equilibrium to another and drifts. Therefore, to remove these low frequency perturbations a local polynomial method will be applied [38]. However, possibly the most significant

difference between our experiment and the past W7-AS experiment is the increased signal-to-noise ratio (SNR) of modern ECE-systems making it possible to detect such non-linearities more easily compared to 20 years ago.

The method is experimentally verified at the Large Helical Device (LHD) using modulated ECRH and ECE to measure the electron temperature fluctuations. In the presented experiment, both the sum and difference interaction terms were detected. Moreover, higher order quadratic interactions were also detected, which is additional evidence for the presence of quadratic non-linearities in the plasma. The spatial distribution of the non-linearity in the amplitude and phase profiles also yielded interesting results showing the applicability of this method.

The paper has the following structure. In the next section, the underlying theoretical concepts are described. Then, the experimental results are described including the spatial distribution of the inter-modulations. In section 4, the consequences for the fundamental harmonics are presented and the spatial distribution of the non-linearity is calculated. Finally, the main conclusions are presented and the experimental interpretation is discussed.

2. Detecting non-linearities

There are several methods available to detect and quantify non-linearities. These methods quantify to what extent the superposition property is valid, which must hold for linear systems. The superposition property can be separated in the homogeneity and additivity properties. The homogeneity or scaling property can be analyzed by changing the amplitude of the perturbation. If the amplitude (local) change of the input perturbation scales linearly with that of the output perturbation the system is linear [39]. The additivity property of linear systems states that the sum of the responses should be the same as the individual responses [40]. A consequence of this additivity property is that the sum of the inputs equals the sum of the individual responses to sinusoidal perturbations. Hence, if the opposite is true and the system contains non-linearities, other "new" components appear at frequencies not part of the original perturbation (excited harmonics). Moreover, new harmonic components also imply that the amplitude and phase of the excited harmonics is changed due to the non-linearities, but this is more difficult to measure than the new components. This section describes the detection and modification of harmonics in detail.

2.1. The Taylor expansion

As perturbative experiments and the Taylor expansion are indissolubly linked, the study of non-linear systems is explained on the basis of the Taylor expansion of the perturbed electron temperature $T(t)$ at some operating point and radial location. In this paper, the perturbed electron temperature $T(\rho, t)$ is analyzed at specific radii ρ , which at some operating point is a non-linear static function h of the plasma parameters $h_0(n_e, P_{dep}(\rho), P_{nbi}(\rho), \dots)$ such as the density n_e , the deposition profile $P_{dep}(\rho)$, heating due to neutral beam injection P_{nbi} , etc. Moreover, $T(\rho, t)$ depends on the waveform or modulation of the perturbative source term $P(t)$, i.e.,

$$T(\rho, t) = h(h_0, P(t)). \quad (1)$$

This non-linear function (1) can be expanded into a Taylor series with respect to time, around the operating point h_0 and $P = 0$ [24], i.e.,

$$T(\rho, t) = \underbrace{h(h_0, 0) + \frac{\partial h(h_0, P)}{\partial P} \Big|_{P=0} P(t)}_{\text{linear contribution}} + \underbrace{\frac{1}{2!} \frac{\partial^2 h(h_0, P)}{\partial P^2} \Big|_{P=0} P^2(t) + \frac{1}{3!} \frac{\partial^3 h(h_0, P)}{\partial P^3} \Big|_{P=0} P^3(t) + \dots}_{\text{non-linear contributions}}.$$

These partial derivatives can also be expressed as gain factors such that (2) becomes (the dependence of K' s on ρ has been omitted)

$$T(\rho, t) = h(h_0) + K_1 \cdot P(t) + K_2 \cdot P^2(t) + K_3 \cdot P^3(t) + \dots, \quad (3)$$

where K_1 contributions are called linear, K_2 non-linear contributions are called quadratic, and those related to K_3 are called cubic non-linearities. Although a Taylor expansion can always be performed, it is only sensible if the non-linearity can be approximated well within a few terms (weak non-linearities).

The source term $P(t)$ generally consists of a number of harmonic components in a perturbative experiment of which two have been explicitly stated, i.e.,

$$P(t) = P_0 + A_1 \cos(f_1 t) + A_2 \cos(f_2 t) + h.o.c., \quad (4)$$

where P_0 is the average power of the perturbation. The higher order components (*h.o.c.*) are harmonic components related to $3f_1, 5f_1, \dots$ and $3f_2, 5f_2, \dots$, which are also induced by a block-wave modulation. The source term (4) is substituted into (3) resulting in the harmonic components of the temperature perturbations at a spatial location ρ given in (5), where (a) is the DC-value; (b) the “linear” responses, which are a combination of the linear contribution and the

quadratic non-linear contribution due to the non-zero average P_0 of the perturbation; ($c-d$) are the harmonic components due to the quadratic part of the Taylor expansion; ($f-k$) are the result of the cubic non-linear part in (2); and (l) are the higher order terms (*h.o.t.*) related to, e.g., K_4 and to perturbed harmonic components different from f_1 and f_2 in (2).

This Taylor expansion shows that higher harmonics will be generated at new frequencies, e.g., $2f_1, 2f_2, 3f_1$, and $3f_2$. It is important to note that the ground harmonics f_1 and f_2 are also modified by the non-linearity. For the case in which two or more sinusoids are used, inter-modulation harmonics are also occurring at $|f_1 - f_2|$, $f_1 + f_2$, $|2f_1 - f_2|$, $|f_1 - 2f_2|$, $2f_1 + f_2$, and $f_1 + 2f_2$. The significance of the contribution depends on the factors K_2 and K_3 . However, these factors also depend on various products of P_0 , A_1 , and A_2 . If P_0 , A_1 , and A_2 are sufficiently small the response to the perturbation can be seen as linear (small perturbation theory). This is because the square and cubic powers of A_1 and A_2 make the contributions negligible. The dependence on P_0 is the result of a perturbation with a heat source. As input power cannot become negative the perturbation is not around the equilibrium but on top of the equilibrium. This means that the equilibrium and harmonic components are modified by P_0 . As the modification of f_1 (and f_2) is of the form $2K_2 P_0 A_1$ this term can significantly modify the assumed linear responses. It is also possible to attribute P_0 to the function h_0 . However, this means that when the type of modulation, e.g., duty cycle and input power, is changed a different equilibrium is studied, as is explained above. As such, any change made to the input can technically not be compared as being from the same equilibrium without proving that the change does not affect the equilibrium. This is undesirable. Hence, we include P_0 explicitly. When $P_0 = 0$ ($2K_2 P_0 A_1 = 0$), then the linear profiles will remain unchanged. The same holds in the case $K_2 = 0$. We interpret the change due to P_0 as the non-linear modification of the linear profiles. This aspect is specifically analyzed in this paper.

Here, we will analyze the unperturbed harmonic components and specifically focus on the difference and sum contributions, i.e., $|f_1 \pm f_2|$ as they can be uniquely attributed to the non-linearity. Two alternative approaches to analyze non-linearities are changing the operating point (equilibrium), e.g., [21], and changing the amplitude of the perturbation, e.g., [39]. However, for these methodologies it is difficult to determine the non-linear component uniquely if the single experiment contains non-linear components, i.e., P_0 and K_2 contributions are not negligible in (5b). The reason is that in the case the amplitude of $P(t)$ is changed at the same time P_0 is also changed.

$$\begin{aligned}
 T(t, \rho) &= h(h_0) + K_1 P_0 + K_2 P_0^2 & (a) \\
 &+ (K_1 + 2K_2 P_0) (A_1 \cos(f_1 t) + A_2 \cos(f_2 t)) & (b) \\
 &+ \frac{1}{2} K_2 (A_1^2 \cos(2f_1 t) + A_2^2 \cos(2f_2 t)) & (c) \\
 &+ K_2 A_1 A_2 (\cos((f_1 - f_2)t) + \cos((f_1 + f_2)t)) & (d) \\
 &+ \frac{3}{2} K_3 A_1 A_2 (A_2 \cos(f_1 t) + A_1 \cos(f_2 t)) & (e) \\
 &+ \frac{1}{4} K_3 (A_1^3 \cos(3f_1 t) + A_2^3 \cos(3f_2 t)) & (f) \\
 &+ \frac{3}{4} K_3 A_1^2 A_2 (\cos((2f_1 - f_2)t) + \cos((2f_1 + f_2)t)) & (g) \\
 &+ \frac{3}{4} K_3 A_1 A_2^2 (\cos((f_1 - 2f_2)t) + \cos((f_1 + 2f_2)t)) & (h) \\
 &+ 3K_3 P_0^2 (A_1 \cos(f_1 t) + A_2 \cos(f_2 t)) & (i) \\
 &+ \frac{3}{2} K_3 P_0 (A_1^2 (1 + \cos(2f_1 t)) + A_2^2 (1 + \cos(2f_2 t))) & (j) \\
 &+ 3K_3 P_0 A_1 A_2 (\cos((f_1 + f_2)t) + \cos((f_1 - f_2)t)) & (k) \\
 &+ h.o.t & (l)
 \end{aligned} \tag{5}$$

Consequently, the amplitude of the main harmonic components is also changed. In the case of changing the operating point, simultaneously K_2 is modified as it depends on the operating point. As P_0 is not negligible the perturbed harmonic components f_1 and f_2 are also modified differently due to the operating point K_2 (see (5b)). Hence, to apply these two analysis methods such contributions need to be taken into account or the linearity of the experiment needs to be validated, e.g., by analyzing higher harmonic components, as will be done here. Although the Taylor expansion is straightforward in explaining how the analysis works, it is not able to describe memory effects using K_1 and K_2 . Instead, a generalization of (5) known as the Volterra series [25] is used which includes these memory effects.

2.2. Volterra series

Volterra series are used to analyze the amplitude of the non-linear contributions and their spatial distribution dynamically. Due to transport there is a delay between the induced perturbation and observed fluctuations measured at different radial locations. This effect is also known as (fading) memory. As the coefficients K_1 and K_2 in (5) are static, they are unable to describe this memory effect, hence, Volterra series are necessary.

The number of terms that need to be considered in the Volterra series (or Taylor expansion) depends on the specific experimental conditions. In the experiment presented in this paper, third order (cubic) non-linear contributions were not observed at their corresponding discrete frequencies. Therefore, it suffices to use a second order Volterra series, which is equivalent in the Taylor expansion to setting all K_3 and higher contributions to zero. Hence, a second order Volterra series is introduced [41, 42], which only considers the relevant discrete harmonic components due to linear

and non-linear quadratic components, i.e.,

$$\begin{aligned}
 \Theta(\rho, k) &= G^{(1)}(\rho, k) U(k) + \\
 &\sum_{k_1=-N+k}^N G^{(2)}(\rho, k_1, k - k_1) U(k_1) U(k - k_1), \tag{6}
 \end{aligned}$$

where $\Theta(\rho, k) = \mathcal{F}(T(\rho, t))$ and $U(k) = \mathcal{F}(u(t))$ with \mathcal{F} denoting the Fourier transform. The frequency is defined here as multiples k of the fundamental frequency such that $k = 1$ corresponds to the lowest frequency present in $\Theta(\rho, k)$ and $k = 0$ to the DC-component. The highest frequency that must be considered is denoted by N . Note that k should not to be confused with the spatial wave number. The Volterra kernels $G^{(1)}$ and $G^{(2)}$ are the complex and frequency dependent equivalents of K_1 and K_2 . $G^{(2)}$ has a three dimensional dependence on the spatial coordinate ρ and k_1 and k . In practice, separate $G^{(2)}$ s are calculated at the radial locations ρ where the temperature is measured. Hence, the Volterra series is only an approximation over time and not over space. The proper choice to define $U(k)$ is to use the power dependent part of the perturbation $u(t) = P(t)$ as has been used in the Taylor expansion in (5). The deposition profile is part of $G^{(1)}$ and $G^{(2)}$ as the input is purely the time dependent part of the perturbation. Alternatively, we can assume that the heat is locally absorbed such that the temperature at the deposition location can be used instead as input, i.e., $u(t) = T_d(\rho_0, t)$. The input $U(k)$ is then defined by $\Theta_d(\rho, k) = \mathcal{F}(T_d(\rho_0, t))$. This allows us to analyze the spatial dependence of the non-linearity. The kernels capture the underlying physics (including the deposition location in case of P) and can be fitted to a large class of non-linear physical descriptions.

As both $G^{(1)}$ and $G^{(2)}$ depend on the underlying physics, (6) will not change when changing the input $U(k)$ from power to temperature but the internal structure or values of $G^{(1)}$ and $G^{(2)}$ will change. The long term goal is to match the estimated values of $G^{(1)}$ and $G^{(2)}$, which we estimate here, to those derived

from physics. The kernel $G^{(1)}$ is simply the transfer function, which is specifically defined for various transport models, as is explained [43]. However, as it is unclear what the underlying physics are, we will not try to match $G^{(1)}$ and $G^{(2)}$ against simulations here. Rather, we will focus on their estimation from measurement data and derive conclusions from calculations using the general Volterra series.

3. Experimental results

In this section, the experimental results are presented. First, the experimental conditions and the expected inter-modulations are given. Then, the spatial distribution of the non-linearities is studied.

Unfortunately, here only two periods are present thus rendering the measure of variance unreliable because at least three periods must be used to estimate the variance [44].

3.1. Set-up and experimental conditions

Experimental results in this paper are presented for the Large Helical Device (LHD) [45]. LHD's major radius $R_{major} = 3.5 \sim 3.9$ m and effective (averaged) minor radius is $a_{99} = 0.6$ m such that ρ is defined by r_{eff}/a_{99} where r_{eff} denotes the effective radius [46].

L-mode plasmas were analyzed with a magnetic field strength of 2.75 T at the magnetic axis $R_{ax} = 3.6$ m. This plasma is sustained using two tangential co/counter neutral beams of total 10 MW, with near zero overall beam driven current. The line-averaged density is approximately $0.9 \cdot 10^{19} \text{ m}^{-3}$. As LHD is a heliotron-type machine, it is free from macroscopic magneto-hydrodynamic instabilities such as sawteeth and neo-classical tearing modes. Consequently, these instabilities cannot disturb the pure plasma transport studies.

Two gyrotrons 77 GHz 5.5U (P_{i1}) and 82.7 GHz (P_{i2}) were used only for plasma initiation. In the steady-state phase of the discharge, EC waves of approximately 2×0.3 MW are injected from the low magnetic field side using the horizontal port launchers called 2Oll for 154GHz 2nd X-mode (P_1) and 2Olr for 77GHz 1st O-mode (P_2) [47]. They are operated to create symmetric power (block-type) modulated EC waves which generate electron heat pulses and fundamental frequencies of $f_1 = 11.11$ Hz (P_1) and $f_2 = 14.29$ Hz (P_2) such that $k = 1$ corresponds to 1.59 Hz (see Fig. 1). Consequently, $k = 7$ corresponds to $f_1 = 7 \cdot 1.59$ Hz and $k = 9$ corresponds to $f_2 = 9 \cdot 1.59$. For inter-modulation $f_1 + f_2$, $k = 7 + 9 = 16$ and for $|f_1 - f_2|$, $k = |7 - 9| = 2$.

The deposition locations were chosen such that both are around $\rho = 0.2$. Although ray-tracing results are available, they were inconsistent with any of the

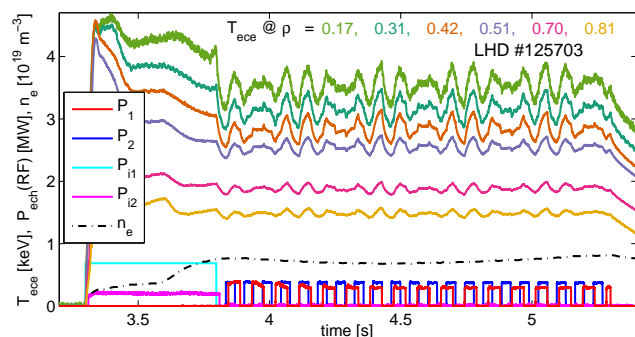


Figure 1. (color) Overview of LHD discharge #125703 showing the time-traces of the calibrated launched EC wave power generated by four gyrotrons; the electron temperature perturbations at different ρ measured with ECE; and the line-averaged density n_e . Gyrotrons P_{i1} and P_{i2} are only used for plasma initiation.

minima or maxima in the amplitude and phase profiles of this discharge. Moreover, in #125699, which is similar to #125703, both 77 GHz 2Olr and 154 GHz 2Oll are applied but at different time-instances of the discharge. This allows us to separately analyze the deposition profiles. The center of deposition, i.e., the maxima of the amplitude of the temperature profiles are clearly also inconsistent with the calculated deposition locations. Hence, the conclusion is that the deposition location estimates based on ray-tracing of 77 GHz 2Olr are inaccurate and hence will not be used in this paper.

Based on the amplitude profiles the deposition profile was probably around $\rho = 0.2$. The electron temperature was measured using electron cyclotron emission (ECE) by a 28-channel radiometer [48] and calibrated using Thomson scattering [49]. The measured electron temperature has been checked for a non-thermal component due to energetic electrons, which are maximally 20% of the ECE signal. An overview of the experimental conditions can be found in Fig. 1. Before the impact of non-linearities can be analyzed, first the existence of $G^{(2)}$ needs to be shown through the existence of a contribution at $2f_1$, $2f_2$, $|f_1 \pm f_2|$.

3.2. Inter-modulation

The corresponding Fourier transforms of the power modulation and the calibrated ECE-temperature measurement can be found in Fig. 2. Fig. 2(a) shows 5 main peaks at f_1 , f_2 , $3f_1$, $3f_2$, and $5f_1$. These correspond to a modulation pattern with duty cycle 50%. Based on this modulation pattern it is expected that no harmonic components are present at $2f_1$, $2f_2$, $4f_1$, and $4f_2$.

In Tab. 1, the main expected harmonic components from linear and non-linear contributions are pre-

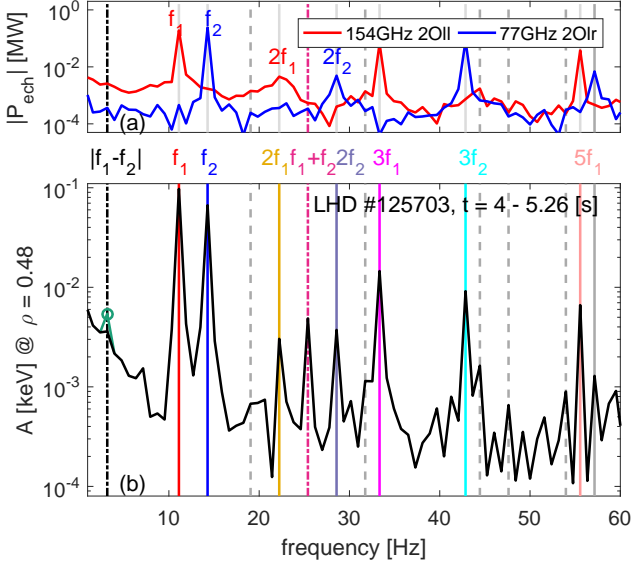


Figure 2. (color) Amplitude spectra of (a) the calibrated EC power and (b) the ECE-measurements at $\rho = 0.48$. The solid lines show the contributions at the perturbed harmonics. The dashed-dotted lines show the locations of the primary inter-modulations and the grey-dashed lines show the secondary inter-modulations. The green circle at $|f_1 - f_2|$ shows the amplitude of $|f_1 - f_2|$ after applying the local polynomial method, which corrects for non-periodic errors in the spectra.

sented based on (5). The two dominant non-linear components are expected at the inter-modulation frequencies 3.17 Hz and 25.40 Hz, and double harmonics 22.22 Hz and 28.57 Hz or (d), (e), and (c) in (5), respectively.

Unfortunately, it is difficult to achieve an exact timing of power outputs of the gyrotrons resulting in a deviation from the 50% duty cycle. This can be seen in Fig. 2(a) by the presence of peaks at $2f_1$ and $2f_2$. If the duty cycle were to be exactly 50%, the amplitude at these frequencies would be zero (noise level). Consequently, amplitude contributions above the noise level at $2f_1$ and $2f_2$ would originate only from non-linear contributions (see (5)). However, as the duty cycle deviates from 50%, the source also contributes to the measured amplitude at $2f_1$ and $2f_2$. Therefore, the measured amplitude at $2f_1$ and $2f_2$ is a combination of the small contribution originating directly from the source and the quadratic non-linear contributions. This makes $2f_1$ and $2f_2$ less reliable for the detection of non-linearities (5). Instead, the inter-modulation frequencies $|f_1 \pm f_2|$ are chosen such that they do not coincide with harmonics present in the original perturbation, as can be seen in Fig. 2(a). In addition, the frequencies f_1 and f_2 are chosen such that $|f_1 \pm f_2|$ are sufficiently small to reduce the effect of the thermal transport on $|f_1 \pm f_2|$.

The corresponding amplitude spectrum at $\rho =$

0.48 is shown in Fig. 2(b). As expected, the strongest harmonic components are at f_1 , f_2 , $3f_1$, and $3f_2$. The next three strongest harmonic components are $f_1 + f_2$, $2f_2$, and $2f_1$, which are far above the noise level ($\approx 4 \cdot 10^{-4}$ keV). The large harmonic component at $f_1 + f_2$ proves that a non-linearity exists and is measurable. This is further supported by the presence of secondary quadratic components at $|3f_1 \pm f_2|$ and $|f_1 \pm 3f_2|$.

The complementary modulation $|f_1 - f_2|$ cannot be recognized due to non-periodic slow temperature drifts and the effect of the unforced response due to a change of equilibrium. Therefore, a correction technique called the local polynomial method (LPM) is applied, which corrects the Fourier spectra for such errors. This LPM technique has been applied successfully to numerous measurements outside fusion research [50, 51, 52, 53] and is explained in more detail in [54].

Cubic non-linearities are not detected at the inter-modulations as the harmonic contributions described in Tab. 1 are too small to be detected. There seems to be only one exception at 39.68 Hz ($2f_2 + f_1$), but it is not present at the other spatial locations. All the secondary quadratic components are present at $3f_1 \pm f_2$ and $f_1 \pm 3f_2$. Only $|f_1 - 3f_2|$ is difficult to detect, but when the LPM is applied the amplitude increases significantly. A strong peak is also observed at 44.44 Hz. This is also a quadratic contribution due to $3f_1 + f_1$ and $3f_2 + f_2$, but it can also be due to a non-linear contribution of the quasi-linear contribution $2(2f_1)$ and $2(2f_1)$. In addition, many other different amplitude peaks can be observed, which are relatively small in amplitude. These can originate from several non-linear interactions including those with $5f_1, 7f_1, 5f_2, 7f_2$. All these other harmonic components are presented in Fig. 3.

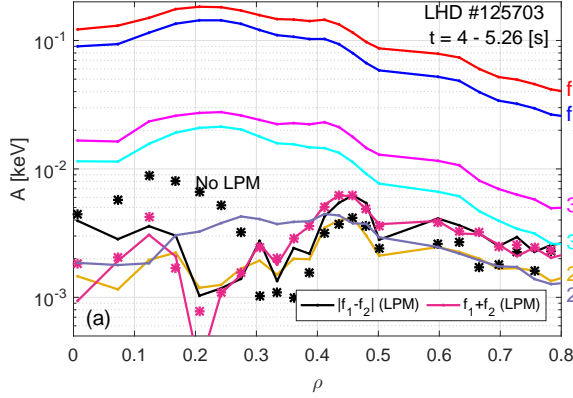
To summarize, there is clear evidence of quadratic non-linear contributions, not only on the primary interactions (f_1 and f_2), but also on the secondary interactions (f_1 and f_2 with $3f_1$ and $3f_2$). On the other hand, there is also a lack of cubic non-linearities, which means that heat transport in this type of plasma discharge can be considered weakly non-linear consistent with the perturbative literature [3].

3.3. Spatial distribution

The spatial distribution of the amplitude is shown in Fig. 3, where only the excited harmonic components and primary non-linear interactions of f_1 and f_2 are shown. As there are no significant cubic non-linearities, these harmonic components are not shown. The spatial distribution of the excited harmonics ($f_1, f_2, 3f_1, 3f_2$) show similar decay profiles with a clear peak around $\rho_0 = 0.2$ corresponding to the chosen deposition

Table 1. Possible non-linear harmonic components due to f_1 and f_2 , with in bold the quadratic interactions only possible due to non-linearities.

Quadratic non-linearities				Cubic non-linearities			
f [Hz]	k	linear	non-linear	f [Hz]	k	linear	non-linear
3.17	2	0	$ f_1 - f_2 $	7.94	5	0	$2f_1 - f_2$
22.22	14	$2f_1$	$2f_1$	11.11	7	f_1	f_1
25.40	16	0	$f_1 + f_2$	14.29	9	f_2	f_2
28.57	18	$2f_2$	$2f_2$	17.46	11	0	$ f_1 - 2f_2 $
Interactions with $3f_1$ and $3f_2$				33.33	21	$3f_1$	$3f_1$
19.05	12	0	$3f_1 - f_2$	36.51	23	0	$2f_1 + f_2$
22.22	14	$2f_1$	$3f_1 - f_1$	39.68	25	0	$f_1 + 2f_2$
28.57	18	$2f_2$	$3f_2 - f_2$	42.86	27	$3f_2$	$3f_2$
31.75	20	0	$ f_1 - 3f_2 $	Interactions with $3f_1$ and $3f_2$			
44.44	28	$4f_1$	$f_1 + 3f_1$	$2f_1 \pm 3f_2$		$2f_1 \pm 3f_1$	
47.62	30	0	$3f_1 + f_2$	$2f_2 \pm 3f_2$		$3f_1 \pm 2f_2$	
53.97	34	0	$f_1 + 3f_2$	$f_1 \pm 6f_2$		$f_1 \pm 6f_1$	
57.14	36	$4f_2$	$3f_2 + f_2$	$f_2 \pm 6f_2$		$6f_1 \pm f_2$	

**Figure 3.** (color) Amplitude profile of the main harmonics as function of the spatial location. The solid lines of $f_1 + f_2$ and $|f_1 - f_2|$ show the estimates compensated with the LPM method. The stars show the same amplitudes without correction.

location ρ_0 . This implies that the bulk of the heat is deposited at this spatial location. Fig. 3 shows at ρ_0 in the amplitude of $|f_1 \pm f_2|$ a clear minimum. Consequently, at this radial location $G^{(2)} \approx 0$, $K_2 \approx 0$, respectively. We expect the non-linearity to originate from the heat pulse propagation and not to originate in the transfer of heat from the source to the plasma. Conversely, if the heat transfer from source to the plasma does not generate non-linear contributions, the radial location where the non-linear component is zero is the deposition location. The absence of a non-linear contribution at the radial location of the probable deposition location supports our expectation that the deposition location is indeed ρ_0 and it also implies that the non-linearity is generated by the heat pulse propagation and not by the heat sources directly. Otherwise, a significant non-linear component would

be expected at all radii including ρ_0 .

A small bump can also be observed at $\rho = 0.42$ in these profiles. Its origin is likely to be from the non-linearity. Studying the radial profile in Fig. 2(b) shows a weak contribution of $|f_1 - f_2|$. The reason is that Fourier coefficients below 5 Hz are dominated by errors due to slow non-periodic fluctuations. These errors can be observed in Fig. 2(b) by the smooth low-frequent decaying function (0.1-6 Hz), which are removed using the local polynomial method. After this removal both amplitude profiles of $|f_1 \pm f_2|$ are similar and show a clear peak around $\rho = 0.45$ and a clear minimum at $\rho = 0.2$. The amplitude increase $\rho < 0.45$ is higher than the amplitude decay $\rho > 0.45$. This is a clear proof that the quadratic non-linearity exists; that it is dominant at $\rho = 0.45$; and that at this frequency range the amplitude difference between $|f_1 \pm f_2|$ is small showing little dynamics.

The primary non-linearity will also occur at $2f_1$ and $2f_2$. However, as explained above the non-linear contributions at $2f_1$ and $2f_2$ are mixed with linear contributions. From the frequency spectrum in Fig. 2(a) the f_1 contribution is larger than f_2 , thus one expects a stronger non-linear contribution on $2f_1$ than on $2f_2$. The amplitude profiles of $2f_1$ and $2f_2$ also show a non-linear component at $\rho = 0.45$ and a similar decay as $|f_1 \pm f_2|$. The harmonic $2f_2$ behaves more similar to the excited harmonics. On the other hand, its amplitude decay around $\rho = 0.45$ is not present. After this point its amplitude decay is almost identical to that of $2f_1$. Most secondary interactions show some similarity to the profiles of $|f_1 \pm f_2|$, but most of them are too small to draw unambiguous conclusions. The secondary quadratic interactions are shown in Fig. 4 including the cubic components, which are significantly smaller than the inter-modulation components. Hence,

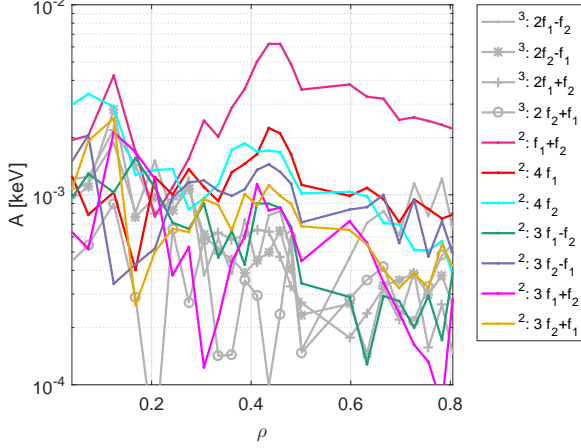


Figure 4. (color) Amplitude profile of non-linear interactions not presented in Fig. 3. Except for $f_1 + f_2$ which is used as a reference. The amplitude profiles labeled with ² belong to quadratic non-linear interactions and those labeled with ³ belong to cubic non-linear interactions. The corresponding frequencies can be found in Tab. 1. It is clear that those belonging to cubic non-linear interactions are small and can be considered negligible. Those belonging to quadratic non-linear interactions depending on the harmonic and if it concerns large or small amplitude inter-modulations are visible.

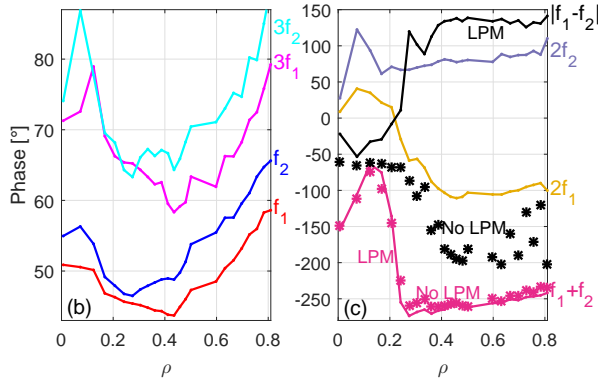


Figure 5. (color) Phase profiles of the main harmonics with (left) the harmonics due to dominant perturbations and (right) harmonics due to dominant non-linearities ($|f_1 \pm f_2|$) and mixed harmonics ($2f_1, 2f_2$). The lines for $|f_1 \pm f_2|$ are LPM compensated, the stars are again without compensation. The phases are compensated w.r.t. the perturbation sources and unwrapped, which only changes the profile height.

the third order components can be neglected.

3.4. Phase profile

The phase profiles are presented in Fig. 5, where the profiles influenced and generated by non-linear interactions are plotted separately from the excited harmonic components.

The harmonics generated by non-linearities $|f_1 \pm f_2|$ show a phase jump at the maximum of the

amplitude profiles of the excited harmonics. The phase jump is approximately 180° , which corresponds to a sign-change. This phase change is opposite for $|f_1 \pm f_2|$. This jump can also be observed in the harmonics $2f_1$ and $2f_2$, but it is not very strong, as it is mixed with the linear contributions. This is also in accordance to the amplitude profile. On the other hand, $2f_1$, which seems most sensitive to the non-linearity, shows a change of almost 150° in the region $\rho = 0.07 - 0.44$.

The phase profiles of f_1 and $3f_1$ have a minimum at $\rho = 0.44$. However, that of f_1 shows a flattening between $\rho = 0.2$ and $\rho = 0.44$. The phase profile of f_2 has a minimum at $\rho = 0.2$ and a lesser minimum at $\rho = 0.44$. Interestingly, $3f_2$ has two minima, one the probable deposition location ρ_0 , and the other at $\rho = 0.44$. At first sight these can be interpreted as two absorption points. However, it is unlikely that both gyrotrons have a second deposition at exactly the same location, e.g., due to re-absorption. Moreover, the amplitude profile with only one clear maximum would be inconsistent with such an observation of a second heating point at $\rho = 0.44$, nor is it consistent with ray-tracing calculations. A much more plausible cause is that the phase change is caused by the non-linearity, which is also consistent with the growing inter-modulation amplitude at this spatial location. This is discussed further and analyzed in the next section.

4. Impact and strength of non-linear contributions

This section shows how to reconstruct the linear profiles of the excited harmonics f_1 and f_2 based on Volterra kernels. In addition, this section explains why the measured amplitudes at $|f_1 \pm f_2|$ are not representative for the local non-linearity of the plasma. In the last part of this section, we try to calculate the local amount of non-linearity of the plasma, which is independent of the size and location of the perturbation.

4.1. Calculation second order Volterra kernels

The non-linearity not only has an impact on the inter-modulation frequencies, but can also have a significant impact on the excited harmonics such as f_1 and f_2 . Here the effect of a change of equilibrium on the amplitude and phase profiles of f_1 and f_2 is studied from two reference points, i.e., the source $P(t)$ and the temperature perturbation at the deposition location $T_d(t)$.

Only quadratic non-linear components have been observed. Hence, significant non-linear distortions at f_1 and f_2 are only expected to originate from

the steady-state value of the perturbation. This is described by (5b), which in terms of the Volterra series is given by

$$\Theta(\rho, 7) = \left(\underbrace{G^{(1)}(\rho, 7)}_{\text{linear}} + \underbrace{2G^{(2)}(\rho, 7, 0)U(0)}_{\text{non-linear modification}} \right) U(7). \quad (7)$$

for f_1 ($k=7$). The measured amplitude profile $|\Theta(\rho, 7)|$ (f_1) is a combination of the linear response and the non-linear modification. Therefore, to calculate the linear profiles the non-linear contribution $G^{(2)}$ needs to be subtracted from $\Theta(\rho, 7)$ in (7), i.e.,

$$\begin{aligned} \Theta_{lin}(\rho, 7) &= G^{(1)}(\rho, 7)U(7) \\ &= \Theta(\rho, 7) - 2G^{(2)}(\rho, 7, 0)U(0)U(7). \end{aligned} \quad (8)$$

Although we do not know $G^{(2)}(\rho, 7, 0)$ in (7) at $(7, 0)$, we can make an approximation based on estimates of $G^{(2)}$ at the inter-modulation frequencies $G^{(2)}(\rho, 9, -7)$ and $G^{(2)}(\rho, 9, 7)$, i.e., $k=2$ ($|f_1 - f_2|$)

$$\Theta(\rho, 2) = 2G^{(2)}(\rho, 9, -7)U(9)U(-7), \quad (9)$$

where $U(-7) = \bar{U}(7)$ (complex conjugate) and $k=16$ ($|f_1 + f_2|$)

$$\Theta(\rho, 16) = 2G^{(2)}(\rho, 9, 7)U(9)U(7). \quad (10)$$

As $U(2)$ and $U(16)$ are zero for $P(t)$ and $T_d(t)$, $G^{(1)}$ does not appear in (9) and (10). If we assume that the kernel $G^{(2)}$ is constant at all frequency combinations, i.e., $G^{(2)}(\rho, 9, 7) = G^{(2)}(\rho, 9, -7) = G^{(2)}(\rho, 7, 0) = G^{(2)}(\rho, 9, 0)$, the linear response can be calculated from (8). Therefore, first the kernels $G^{(2)}$ are calculated to verify this assumption.

Fig. 6(a,b) shows the amplitude and phase of the second order Volterra kernels at the inter-modulation frequencies. The amplitudes are remarkably similar and the phase profiles have a difference of $\approx 90^\circ$ for $\rho > 0.3$ for $u(t) = P(t)$. It is peculiar that the Volterra kernels are changing phase around the deposition location ρ_0 , for which we do not have a physics explanation yet.

The Volterra kernels are also calculated using as reference the temperature perturbation at the deposition location, i.e., $u(t) = T_d(t)$. The mean value of $T_d(t)$ is a combination of the equilibrium $h(h_0)$ and the change due to P_0 as shown in (5a). We are only interested in the change of equilibrium due to T_0 . As in (5a) $K_2P_0^2 \approx 0$, only the contribution due to $T_0 \approx K_1P_0$ is taken into account. This value is ideally calculated from $h(h_0)$ to the average value of the new equilibrium $h(h_0) + T_0$. However, as the original equilibrium temperature $h(h_0)$ is not available the average value of the perturbation $T_0 = \frac{1}{2}\|T_d(t)\|_1 =$

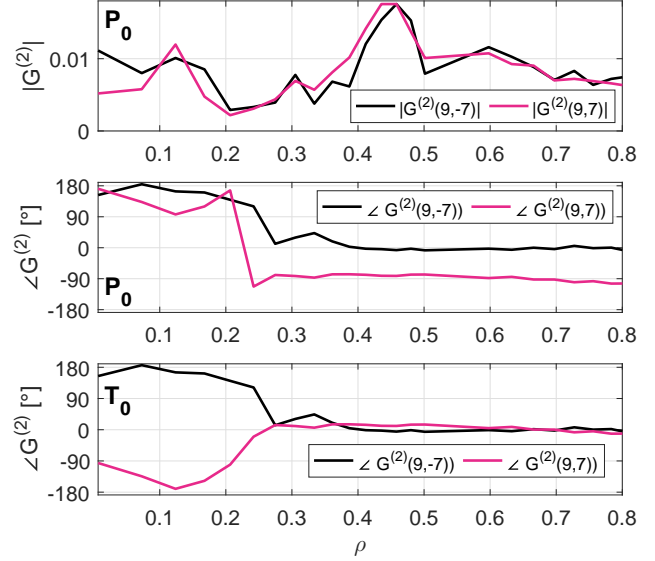


Figure 6. (color) Estimated non-linear global Volterra kernels $G^{(2)}$ calculated using (9) and (10) in case $u(t) = P(t)$ and $u(t) = T_d(t)$. Note that in case $u(t) = T_d(t)$ only the scaling of the amplitude changes (T_0 instead of P_0). Hence, only the phase difference is represented.

0.55 [keV] is used. The phase profiles of the kernels $u(t) = T_d(t)$ are shown in Fig. 6(c). The amplitude profiles of $G^{(2)}$ for $u(t) = T_d(t)$ are not shown as they only differ a scaling factor compared to those shown in Fig. 6(a).

There is no longer a phase difference between the kernels $\rho < 0.3$ when using $T_d(t)$ as reference. Therefore, for $\rho > 0.3$, the kernels $G^{(2)}$ can be considered constant (static) when using $T_d(t)$ as a reference. This allows us to replace the $G^{(2)}$ kernels at the inter-modulation frequencies with those at $G^{(2)}(\rho, 7, 0)$ and $G^{(2)}(\rho, 9, 0)$ necessary to calculate the true linear profiles.

4.2. Non-linear impact on f_1 and f_2

In this subsection, the linear profiles $\Theta_{lin}(\rho, 7)(f_1)$ and $\Theta_{lin}(\rho, 9)(f_2)$ defined in (8) are reconstructed using the temperature perturbation at $T_d(t)$ as reference. Therefore, it is assumed that $G^{(2)}(\rho, 9, 7) = G^{(2)}(\rho, 9, 0)$ and $G^{(2)}(\rho, 9, -7) = G^{(2)}(\rho, 7, 0)$ as was explained in Sec. 4.1. The result is shown in Fig. 7(a-d).

The corrected amplitude profiles of $\Theta_{lin}(\rho, 7)$ and $\Theta_{lin}(\rho, 9)$ have decreased significantly for both the corrections based on $f_1 + f_2$ ($G^{(2)}(\rho, 9, 7)$) and $|f_1 - f_2|$ ($G^{(2)}(\rho, 9, -7)$). In particular, the bump visible at $\rho = 0.41$ has disappeared. The effect of the non-linearity on the phase profile is even more significant as all minima at $\rho = 0.44$ have disappeared in the case of $f_1 + f_2$. This becomes particularly clear when

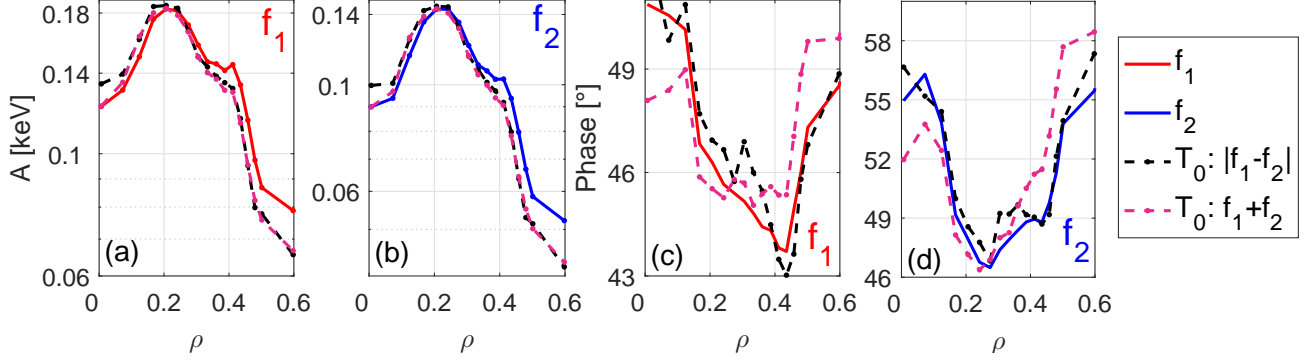


Figure 7. (color) (a-d) Amplitude and phase profiles of f_1 and f_2 of the original measured profiles (full), and the profiles compensated for the non-linearities using $G^{(2)}(7, 9)$ and $G^{(2)}(-7, 9)$ (dashed). They are all calculated from $T_d(\rho_0, k)$ where T_0 is the amplitude of the perturbation in time domain (one-norm). The amplitudes are all consistent with each other (the same holds for the calculation from P_0). The phase shows quite different behavior. Note that the for the calculation using the difference frequencies $|f_1 - f_2|$ an additionally the LPM has been applied.

compared to phase profiles corrected using $|f_1 - f_2|$. These show a different phase profile and strong minima at the location of the non-linearity. However, the profile at $|f_1 - f_2|$ is reconstructed and hence is more error prone.

As both the bump at $\rho = 0.41$ and all minima at $\rho = 0.44$ are absent in the corrected phase profiles, this analysis shows that the profiles of amplitude are consistently modified by the non-linearity. Therefore, these changes in the profiles can lead to misinterpretations because their gradients are used to determine transport coefficients.

The corrected profiles using $u(t) = P(t)$ as a reference can be found in the Appendix. The calculations based on $u(t) = P(t)$ as a reference show similar corrected amplitude profiles and behavior of the phase except for some phase reconstructions. However, as the phase is different using $G^{(2)}(\rho, 9, 7)$ and $G^{(2)}(\rho, 9, -7)$, the assumption to replace $G^{(2)}(\rho, 9, 7)$ and $G^{(2)}(\rho, 9, -7)$ for $G^{(2)}(\rho, 7, 0)$ seems invalid at least for individual cases. Hence, we have chosen to use $T_d(t)$ as a reference instead of $P(t)$.

4.3. The local non-linearity vs. amplitude of inter-modulation frequencies

In this section, we show that the amplitude of the inter-modulation frequencies are not necessarily the radial locations where the plasma is most non-linear. The calculation of $G^{(1)}$ and $G^{(2)}$ only describes global transport from ρ_0 to ρ . Hence, $G^{(2)}$ describes the total amount of non-linearity over the entire domain ρ_0 to ρ . Therefore, if we want to estimate the local amount of non-linearity we should estimate the local non-linear Volterra kernels, called $L^{(2)}$, over a small interval, e.g., $\Delta\rho = \rho_{i+1} - \rho_i$. The difference between the local kernel $L^{(2)}$ and the global Volterra kernel $G^{(2)}$ is shown schematically in Fig. 8.

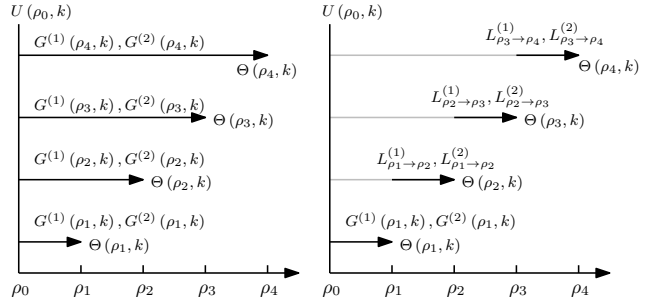


Figure 8. Schematic depiction of the estimation procedure with (right) the method to calculate the Volterra kernels $G^{(1)}$ and $G^{(2)}$ and (left) the method to calculate the local Volterra kernels $L^{(1)}$ and $L^{(2)}$ for different domains $[\rho_i, \rho_{i+1}]$.

The local Volterra kernels over a small interval $\Delta\rho$ follow from the definition in (6) where input $U(k)$ is the temperature at different ρ , i.e.,

$$\begin{aligned} \Theta(\rho_{i+1}, 16) &= L_{\rho_i \rightarrow \rho_{i+1}}^{(1)}(\rho, 16) \Theta(\rho_i, 16) \\ &+ \Theta(\rho_i, 9) \Theta(\rho_i, 7) L_{\rho_i \rightarrow \rho_{i+1}}^{(2)}(9, 7). \end{aligned} \quad (11)$$

$L_{\rho_i \rightarrow \rho_{i+1}}^{(1)}$ describes the linear transport properties of the plasma and $L_{\rho_i \rightarrow \rho_{i+1}}^{(2)}$ the quadratic non-linear transport properties of the plasma. In this representation, $U(k)$ is non-zero at the inter-modulation frequencies for $\rho_i \neq \rho_0$. Consequently, this formula cannot be directly used to calculate the local amount of non-linearity $L_{\rho_1 \rightarrow \rho_2}^{(2)}$ (see discussion below (10)). However, we can use it to interpret the experiments and analyze the measured radial profiles in Fig. 3.

Equation (11) shows that the measured amplitude at $f_1 + f_2$, i.e., $|\Theta(\rho_{i+1}, 16)|$, is a combination of 1) how the local linear transport $L_{\rho_i \rightarrow \rho_{i+1}}^{(1)}$ dissipates the Fourier coefficient $\Theta(\rho_i, 16)$ and 2) a non-linear contribution which is a combination of the plasma

non-linearity $L_{\rho_i \rightarrow \rho_{i+1}}^{(2)}$ and the profiles $\Theta(\rho_i, 7)$ and $\Theta(\rho_i, 9)$ of the main perturbation f_1 and f_2 .

In Fig. 3 it is clearly visible that $\Theta(\rho_i, 7)$ and $\Theta(\rho_i, 9)$ decrease with increasing radius for $\rho > \rho_0$. This means that even if $L_{\rho_i \rightarrow \rho_{i+1}}^{(2)}(9, 7)$ is constant, a decrease in $\Theta(\rho_i, 7)$ and $\Theta(\rho_i, 9)$ will lead to a decrease in amplitude of $\Theta(\rho_{i+1}, 16)$. Therefore, the amplitude profile observed in Fig. 3 can be separated into three phases:

- (i) $0.2 < \rho < 0.45$: The term $\Theta(\rho_i, 9) \Theta(\rho_i, 7) L_{\rho_i \rightarrow \rho_{i+1}}^{(2)}(9, 7)$ dominates over $L_{\rho_i \rightarrow \rho_{i+1}}^{(1)}(\rho, 16) \Theta(\rho_i, 16)$ in (11). Consequently, we will see that the amplitude $|\Theta(\rho_{i+1}, 16)|$ increases. As both $\Theta(\rho_i, 7)$ and $\Theta(\rho_i, 9)$ are large for $\rho < 0.45$, the local non-linear contribution $L_{\rho_i \rightarrow \rho_{i+1}}^{(2)}(9, 7)$ does not need to be large to dominate over $L_{\rho_i \rightarrow \rho_{i+1}}^{(1)}(\rho, 16) \Theta(\rho_i, 16)$.
- (ii) $\rho \approx 0.45$: A maximum occurs when $|\Theta(\rho_{i+1}, 16)| = |\Theta(\rho_i, 16)|$. This means that in (11), the term $\Theta(\rho_i, 9) \Theta(\rho_i, 7) L_{\rho_i \rightarrow \rho_{i+1}}^{(2)}(9, 7)$ matches the decrease in amplitude due to the linear transport (dissipation) $L_{\rho_i \rightarrow \rho_{i+1}}^{(1)}(\rho, 16) \Theta(\rho_i, 16)$ in (11). Consequently, $\rho \approx 0.45$ is not the location where the plasma itself is most non-linear as this is the location where $L_{\rho_i \rightarrow \rho_{i+1}}^{(2)}(9, 7)$ is largest.
- (iii) $\rho > 0.45$: When $\Theta(\rho_i, 7)$ and $\Theta(\rho_i, 9)$ decrease in amplitude, even if the plasma is very non-linear, i.e., $L_{\rho_i \rightarrow \rho_{i+1}}^{(2)}(9, 7)$ is large, the combined term $\Theta(\rho_i, 9) \Theta(\rho_i, 7) L_{\rho_i \rightarrow \rho_{i+1}}^{(2)}(9, 7)$ will be smaller than $L_{\rho_i \rightarrow \rho_{i+1}}^{(1)}(\rho, 16) \Theta(\rho_i, 16)$. Consequently, the linear transport $L_{\rho_i \rightarrow \rho_{i+1}}^{(1)}(\rho, 16) \Theta(\rho_i, 16)$ will dominate over $\Theta(\rho_i, 9) \Theta(\rho_i, 7) L_{\rho_i \rightarrow \rho_{i+1}}^{(2)}(9, 7)$ resulting in a decrease of amplitude of $\Theta(\rho_i, 16)$. However, in Fig. 3 this decrease (spatial amplitude gradient) $|\Theta(\rho_i, 16)|$ is smaller than that of $\Theta(\rho_i, 7)$ and $\Theta(\rho_i, 9)$ suggesting that $L_{\rho_i \rightarrow \rho_{i+1}}^{(2)}(9, 7)$ is a large quantity.

In conclusion the measured amplitude at the intermodulation frequencies is the result of the interplay among the perturbation, the linear transport, and the non-linear transport. Therefore, $L_{\rho_i \rightarrow \rho_{i+1}}^{(2)}$ needs to be estimated to determine where the plasma is most non-linear.

4.4. Calculating the strength of local non-linearity

In this section, we try to answer the question if it is possible to determine the local non-linearity $L^{(2)}$ extensively discussed in the previous subsection. The

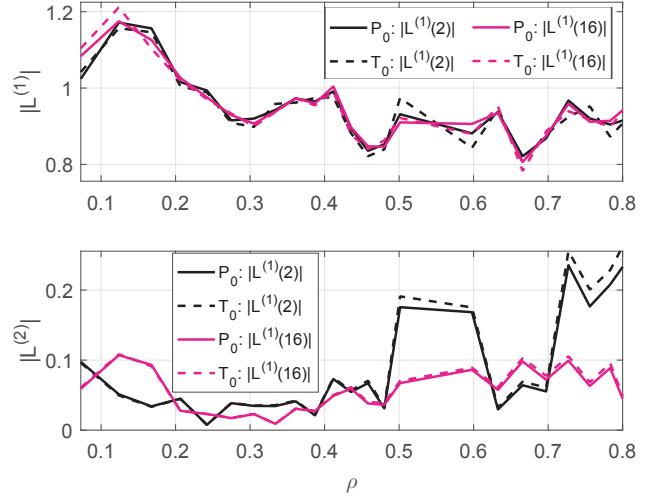


Figure 9. Approximation of the local kernels $L^{(1)}$ and $L^{(2)}$. The local kernels are all calculated via ρ_0 either starting directly from T_0 or via P_0 . This also explains their similarity.

definition (11) can be rewritten as

$$L_{\rho_i \rightarrow \rho_{i+1}}^{(2)}(9, 7) = \frac{\Theta(\rho_{i+1}, 16) - L_{\rho_i \rightarrow \rho_{i+1}}^{(1)}(\rho, 16) \Theta(\rho_i, 16)}{\Theta(\rho_i, 9) \Theta(\rho_i, 7)}. \quad (12)$$

The only unknown in this equation is $L_{\rho_i \rightarrow \rho_{i+1}}^{(1)}(\rho, 16)$. It can be calculated from the global kernels $G^{(1)}$ using the property that when $G^{(2)}$ and $L^{(2)}$ are zero

$$L_{\rho_i \rightarrow \rho_{i+1}}^{(1)}(k) = \frac{G^{(1)}(\rho_{i+1}, k)}{G^{(1)}(\rho_i, k)}. \quad (13)$$

Remember that we do not have the actual $G^{(1)}$, but we have the estimates using the global non-linear kernels $G^{(2)}$. These have been estimated in Sec. 4.1, using additional assumptions on $G^{(2)}$ and heavily rely on a chain of assumptions. In particular, on the assumption that all the heat has been deposited at ρ_0 . If this is not true, this specific analysis may lose validity, for instance, in the presence of non-local transport as has been observed in similar discharges at LHD [30]. The local kernels are shown in Fig. 9, which should be interpreted with care due to the assumptions on the estimation of $G^{(1)}$.

Fig. 9 clearly shows that $L^{(2)}$ is not dominant at the peak in $|f_1 \pm f_2|$ at $\rho = 0.45$, but is increasing with radius. The amplitudes are similar for the local linear kernels $L^{(1)}(2)$ and $L^{(1)}(16)$.

We expect in a local sense $L^{(1)}$ to behave as diffusive transport, i.e., a strong decay as function of ρ and f . This is not the case here. One of the reasons that this is not occurring might be the relative low-frequency at which this transfer function $L^{(1)}$ is measured. The local non-linear component also suffers

from signal-to-noise ratio problems. The reason is that the amplitudes of $\Theta(\rho_i, 7)$ and $\Theta(\rho_i, 9)$ decrease with increasing ρ . Consequently, $L^{(2)}$ becomes unreliable at large radii $\rho \gtrsim 0.6$ due to the lack of non-linear growth of the term $\Theta(\rho_i, 9) \Theta(\rho_i, 7) L_{\rho_i \rightarrow \rho_{i+1}}^{(2)}(9, 7)$ making it difficult to calculate $L_{\rho_i \rightarrow \rho_{i+1}}^{(2)}(9, 7)$.

In summary, mathematically it is valid to calculate the local kernels $L^{(1)}$ and $L^{(2)}$. However, due to the lack of non-linear growth and uncertainty it is unclear if the L profiles are reliable. One indication that the profile might be correct is that the turbulence level, which in LHD can be spatio-temporally resolved using phase contrast imaging (PCI) [55, 56], gives a similar turbulence profile of turbulence as that of the non-linearity. However, more experiments are necessary to show that this relationship exists.

5. Conclusion and discussion

Based on a single perturbative experiment this paper shows that non-linearities exist and can be quantified by the amplitude at the inter-modulation frequencies. Moreover, due to the absence of third and higher order inter-modulation components the non-linearity is weak in this plasma regime. The inter-modulation harmonic components are 1-2 orders smaller in amplitude than the amplitudes of the main harmonic components f_1 and f_2 . As such physical descriptions that have a strong non-linear component do not describe the regime in which these measurements are performed. Moreover, as only a few inter-modulation components are present, the measurements show that a Volterra series can be applied to approximate the non-linearity. The similarity between the kernel values at $f_1 + f_2$ and $|f_1 - f_2|$ is remarkable. In particular, as for this application the modified local polynomial method (LPM) has no relation to $f_1 + f_2$ nor in its calculation or frequency range used. This also shows the value of removing spectral errors at $|f_1 - f_2|$ from the spectra with the LPM.

An important complication when analyzing perturbative experiments using a heat source as perturbation is the non-zero average P_0 of the perturbation. The non-linearity significantly distorts the “linear” amplitude and phase profiles, which are generally used for physics interpretations and thus this can lead to misinterpretations.

It is also shown that it is possible to correct or at least to get an idea of the error in the amplitude and phase profiles. The linear estimates of the amplitude profiles are similar for both reconstructions from $P(t)$ or the temperature $T_d(t)$ at the assumed deposition location. The phase reconstructions vary depending on which correction is used, but all show that they are clearly modified. Based on the information concerning

the sources (deposition, amplitude, phase profiles), the observed non-linearity in the amplitude is not at the deposition locations. This leads us to the conclusion that the inter-modulation frequencies are not fed directly by the source, but are only generated in the process of the heat pulse propagation, i.e., transport. Hence, we have calculated the Volterra kernels from the temperature at the assumed location of deposition to the different temperature locations. Moreover, the significant changes around $\rho \approx 0.42$ can also be interpreted as the equilibrium being very sensitive to changes in the input power P_0 .

The amplitude and phase profiles of the inter-modulation harmonics show that the impact of the non-linearity is distributed with a strong effect around $\rho \approx 0.42$. However, the resulting amplitude and phase at a specific radial location are not only the radial distribution of the underlying physics non-linearity but are the result of a combination of the perturbation, non-linearity, and the perturbation and non-linearity at other radial locations. Therefore, a first attempt is made to reconstruct the non-linearity by estimating the local Volterra kernels. The result shows that there is no longer a strong non-linear peak at $\rho \approx 0.42$. Hence, this supports our conclusion that the non-linearity is distributed. However, as the amplitude is relatively small for large radii, the measurement of the non-linearity becomes unreliable. This needs to be improved in the future. As the analysis method presented here is fully measurement driven through the use of non-parametric Volterra kernels, conclusions can be reached without assuming a specific physics paradigm. The next step is to construct parametric Volterra kernels from various physics models, which can be directly compared to the measured kernels. Note that the kernels $G^{(1)}$ and $G^{(2)}$ can capture also possible non-local transport.

This experimental approach shows great promise for future perturbative transport experiments. However, there is significant room for improvement. The first necessary step is the inclusion of an uncertainty analysis with errors in the frequency domain. In this experiment only two periods were used. These should be increased to at least three and preferably to 7 in order to retain important statistical properties under Gaussian noise assumptions [57]. Secondly, since the non-linear analysis is based on the two inter-modulation harmonics, these should be increased with reasonable signal-to-noise ratios in order to arrive at a better estimate of the Volterra kernel especially in the relevant frequency range. Finally, this experiment is relatively easy to perform in the sense that two modulated (block-wave) sources are necessary. However, if this experiment were to be performed by a single gyrotron with multilevel power modulation, possi-

ble interactions between deposition locations would no longer be relevant and it would be possible to design modulation signals, which can estimate a larger number of frequency points in the kernel, allowing for an even better non-linear interpretation and the possible exclusion of various physics descriptions as the models based on the physics should give the same Volterra kernels.

Finally, in this paper, we have deliberately not assumed a physics model as it is unclear what non-linear physics is causing the inter-modulation components. Instead, we try (based on measurements) to identify what properties the underlying physics (model) must have. Therefore, a general Volterra description is used, which captures the physics in a non-parametric way. If the Volterra kernel has been properly estimated using the above suggestions, the underlying physics model must reproduce the Volterra kernel within its statistical uncertainty.

6. Acknowledgments

Acknowledgments Fruitful discussions with Dr. K. Ida are gratefully acknowledged. This research has been largely performed with a fellowship of the Japan Society for the Promotion of Science (JSPS). This work was in part funded by the Flemish Government (Methusalem Fund, METH1/VUB). ECRH system is supported under grants ULRR701, ULRR801, ULRR804 by NIFS. This work has been carried out within the framework of the EUROfusion Consortium and has received funding from the Euratom research and training programme 2014-2018 under grant agreement No 633053. The views and opinions expressed herein do not necessarily reflect those of the European Commission.

Appendix A. Calculation of non-linear contribution with Volterra series

Volterra series describes the input and output behavior of weakly non-linear systems. In our case the input U is defined as the complex Fourier spectrum of $P(t)$ or the temperature T at $\rho_0 = 0.21$ and the outputs Θ are defined as the complex Fourier coefficients of the temperatures T at the different radii. This means that the dynamics between different measurements are always calculated either directly from $P(t)$ or from the temperature $T_d(t)$ assumed deposition location ρ_0 to the other measurements. This deposition location is also the only location where the inter-modulation harmonics are small and as such it is reasonable to assume that the input consists of only the excited harmonic components. This is also depicted in Fig. 8 (left). Hence, the newly generated harmonics at ρ_0 are

considered negligible and the input is defined as

$$u(t) = U(0) + U(7)e^{i2\pi 7f_0} + U(-7)e^{-i2\pi 7f_0} + U(9)e^{i2\pi 9f_0} + U(-9)e^{-i2\pi 9f_0}. \quad (\text{A.1})$$

In the previous section, it has been established that third order non-linearities have not been detected (see Fig. 2). Therefore, it suffices to only consider second order Volterra kernels. In [41] and (6) the second order Volterra series in the frequency domain is defined as follows

$$\Theta(\rho, k) = \underbrace{G^{(1)}(\rho, k)U(k)}_{\text{linear}} + \underbrace{\sum_{k_1=-N+k}^N G^{(2)}(\rho, k_1, k-k_1)U^{(2)}(k_1, k-k_1)}_{\text{quadratic}}, \quad (\text{A.2})$$

where $k = 1, \dots, N$ with k the harmonic number; $G^{(1)}(k)$ is the first order kernel; $G^{(2)}(k_1, k-k_1)$ is the second order kernel; N is the product of the highest harmonic number appearing in the output with the highest non-linear contribution ($N = 9 \cdot 2$); and $U^{(2)}(k_1, k_2)$ is the second-order poly-spectrum defined as

$$U^{(2)}(k_1, k_2) = U(k_1) \cdot U(k_2). \quad (\text{A.3})$$

The fundamental frequency of one period is $f_0 = 1.54$ Hz. Consequently, f_1 , f_2 , $|f_1 - f_2|$, and $f_1 + f_2$ in terms of harmonic numbers are $k = 7, 9, 2, 16$, respectively.

Appendix A.1. Calculation linear contribution

The total contributions on the different harmonics can be calculated using (4) by substituting the harmonic number, e.g., $k = 7$

$$\Theta(\rho, 7) = G^{(1)}(\rho, 7)U(7) + \sum_{k_1=-11}^{18} G^{(2)}(\rho, k_1, 7-k_1)U(k_1) \cdot U(7-k_1), \quad (\text{A.4})$$

which simplifies to

$$\Theta(\rho, 7) = G^{(1)}(\rho, 7)U(7) + 2G^{(2)}(\rho, 0, 7)U(0)U(7) \quad (\text{A.5})$$

because the product in (A.3) and (A.4) is only non-zero for $k_1 = 0$. Also, the other combinations can be calculated, which results in the following non-zero contributions for $k = 9$

$$\Theta(\rho, 9) = G^{(1)}(\rho, 9)U(9) + 2G^{(2)}(\rho, 0, 9)U(0)U(9), \quad (\text{A.6})$$

for $k = 2$

$$\Theta(\rho, 2) = 2G^{(2)}(\rho, 9, -7) U(9) U(-7) \quad (\text{A.7})$$

and for $k = 16$

$$\Theta(\rho, 16) = 2G^{(2)}(\rho, 9, 7) U(9) U(7). \quad (\text{A.8})$$

Other non-zero contributions such as the complex conjugates Fourier coefficients of the here shown harmonics are not presented, which also holds for $\Theta(\rho, 14)$ and $\Theta(\rho, 18)$.

The Volterra kernel $G^{(1)}$ equals the linear transport in terms of a transfer function as defined in [43]. Hence, this kernel $G^{(1)}$ is frequency dependent and represents the best true linearized dynamics whereas $G^{(2)}$ acts as a non-linear error on this measurement. Note that following the definitions here these kernels $G^{(1)}$ and $G^{(2)}$ do not depend on the amplitude of the inputs. Although it is not possible to directly calculate $G^{(2)}(\rho, 0, 9)$ and $G^{(2)}(\rho, 0, 7)$ in (A.5) and (A.6), it is possible to calculate the kernels values at $G^{(2)}(\rho, 9, -7)$ and $G^{(2)}(\rho, 9, 7)$ using the inter-modulations in (A.7) and (A.8), i.e.,

$$G^{(2)}(\rho, 9, -7) = \frac{1}{2} \frac{\Theta(\rho, 2)}{U(9) U(-7)}, \quad (\text{A.9})$$

where the conjugate can be used $\overline{U(7)} = U(-7)$ and

$$G^{(2)}(\rho, 9, 7) = \frac{1}{2} \frac{\Theta(\rho, 16)}{U(9) U(7)}. \quad (\text{A.10})$$

This also shows why the inter-modulation components are so important as they offer a near independent estimation of the second order kernel. The values of this kernel are plotted in Fig. 6. It clearly shows that the amplitude differences and phase differences for $\rho > 0.3$ between $G^{(2)}(9, -7)$ and $G^{(2)}(9, 7)$ are small. Hence, we conclude that it is reasonable to assume that the points $G^{(2)}(0, f_1)$ and $G^{(2)}(0, f_1)$ are close to $G^{(2)}(9, -7)$ and $G^{(2)}(9, 7)$. Consequently, they can be replaced by their complex values. It is then possible to calculate the linear contributions by rewriting (A.5) resulting in

$$G^{(1)}(\rho, 7) \approx \frac{\Theta(7, \rho)}{U(7)} - 2G^{(2)}(\rho, 0, 7) U(0) \quad (\text{A.11})$$

and for $k = 9$

$$G^{(1)}(\rho, 9) \approx \frac{\Theta(9, \rho)}{U(9)} - 2G^{(2)}(\rho, 0, 9) U(0). \quad (\text{A.12})$$

This allows us to calculate the purely linear contribution $\Theta_{lin}(\rho, k)$

$$\Theta_{lin}(\rho, k) = G^{(1)}(\rho, k) U(k), \quad (\text{A.13})$$

which only depend upon $G^{(1)}$. This calculation is used to produce Fig. 7 and Fig. A1 in case of $u(t) = T_d(t)$ and $u(t) = P(t)$, respectively.

Appendix A.2. Calculation non-linear contribution

In the previous sub-section, the linear contributions have been calculated. Here, using $G^{(1)}$ from (A.13) the local non-linear contribution can be estimated, which is called $L_{\rho_i \rightarrow \rho_{i+1}}^{(2)}$. This is graphically depicted in Fig. 8(right). Locally the inter-modulation $f_1 + f_2$ ($k = 16$) is a combination of a linear and non-linear component. For instance, if the Volterra kernels between ρ_1 and ρ_2 are considered, then based on (6) this results in

$$\begin{aligned} \Theta(\rho_2, 16) &= L_{\rho_1 \rightarrow \rho_2}^{(1)}(16) \Theta(\rho_1, 16) \\ &+ 2L_{\rho_1 \rightarrow \rho_2}^{(2)}(9, 7) \Theta(\rho_1, 9) \Theta(\rho_1, 7), \end{aligned} \quad (\text{A.14})$$

where the temperature measurement at ρ_1 is defined as $\Theta(\rho_1, 16)$, which consist of four harmonic components unlike $U(16)$. Similar to (A.13), the linear change between ρ_1 and ρ_2 of the Fourier coefficients is defined as

$$\Theta_{lin}(\rho_2, 16) = L_{\rho_1 \rightarrow \rho_2}^{(1)}(16) \Theta_{lin}(\rho_1, 16). \quad (\text{A.15})$$

In addition, based on (A.13) the following relationships hold

$$\begin{aligned} \Theta_{lin}(\rho_1, 16) &= G^{(1)}(\rho_1, 16) U(16) \\ \Theta_{lin}(\rho_2, 16) &= G^{(1)}(\rho_2, 16) U(16). \end{aligned} \quad (\text{A.16})$$

Combining the relationships in (A.16) and (A.15), the local Volterra kernel can be calculated

$$L_{\rho_1 \rightarrow \rho_2}^{(1)}(16) = \frac{G^{(1)}(\rho_2, 16)}{G^{(1)}(\rho_1, 16)}. \quad (\text{A.17})$$

Similarly all the $L_{\rho_i \rightarrow \rho_{i+1}}^{(1)}(16)$ can be calculated. The local non-linear dependence can now be calculated between ρ_1 and ρ_2 based on (A.14) substituting (A.17), which results in

$$\begin{aligned} L_{\rho_1 \rightarrow \rho_2}^{(2)}(9, 7) &= \\ \frac{1}{2} \frac{G^{(1)}(\rho_1, 16) \Theta(\rho_2, 16) - G^{(1)}(\rho_2, 16) \Theta(\rho_1, 16)}{G^{(1)}(\rho_1, 16) \Theta(\rho_1, 9) \Theta(\rho_1, 7)}. \end{aligned} \quad (\text{A.18})$$

This is generalized for $k = 16$

$$\begin{aligned} L_{\rho_i \rightarrow \rho_{i+1}}^{(2)}(9, 7) &= \\ \frac{1}{2} \frac{G^{(1)}(\rho_i, 16) \Theta(\rho_{i+1}, 16) - G^{(1)}(\rho_{i+1}, 16) \Theta(\rho_i, 16)}{G^{(1)}(\rho_i, 16) \Theta(\rho_i, 9) \Theta(\rho_i, 7)} \end{aligned} \quad (\text{A.19})$$

and for $k = 2$

$$\begin{aligned} L_{\rho_i \rightarrow \rho_{i+1}}^{(2)}(9, -7) &= \\ \frac{1}{2} \frac{G^{(1)}(\rho_i, 2) \Theta(\rho_{i+1}, 2) - G^{(1)}(\rho_{i+1}, 2) \Theta(\rho_i, 2)}{G^{(1)}(\rho_i, 16) \Theta(\rho_i, 9) \Theta(\rho_i, -7)} \end{aligned} \quad (\text{A.20})$$

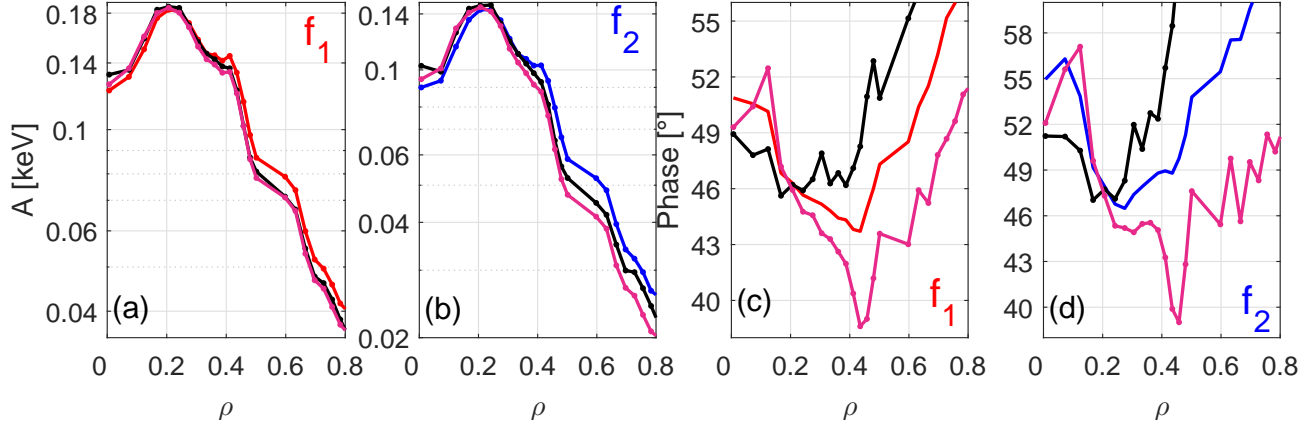


Figure A1. (color) (a-d) Amplitude and phase profiles of f_1 and f_2 of the original measured profiles (full), and the profiles compensated for the non-linearities Θ_{lin} using $G^{(2)}(7, 9)$ and $G^{(2)}(-7, 9)$ (colors correspond to Fig. 7, but here P_0 is used). They are all calculated from $P(t)$. The phase shows quite different behavior. Before calculating the compensated profiles using $|f_1 - f_2|$, the profiles of $|f_1 - f_2|$ have been corrected using the LPM method.

This allows the calculation of the local strength of the non-linearity, which resulted in Fig. 9.

References

- [1] Van Milligen B P, Hidalgo C *et al.* 1995 *Phys. Rev. Lett.* **74** 395–398
- [2] Ryter F, Dux R, Mantica P and Tala T 2010 *Plasma Phys. Control. Fusion* **52** 124043
- [3] Lopes Cardozo N J 1995 *Plasma Phys. Control. Fusion* **37** 799
- [4] Ida K, Inagaki S, Sakamoto R, Tanaka K, Funaba H, Takeiri Y, Ikeda K, Michael C, Tokuzawa T, Yamada H, Nagayama Y *et al.* 2006 *Phys. Rev. Lett.* **96**(12) 125006
- [5] Giannone L, Erckmann V, Gasparino U, Hartfuss H J, Kuhner G, Maassberg H, Stroth U and Tutter M 1992 *Nucl. Fusion* **32** 1985
- [6] Hogewij G M D 2010 *Fusion Sci. Technol.* **57** 357–363
- [7] Ryter F, Tardini G, Luca F D, Fahrbach H U, Imbeaux F, Jacchia A, Kirov K, Leuterer F, Mantica P, Peeters A, Pereverzev G, Suttrop W and the ASDEX Upgrade Team 2003 *Nucl. Fusion* **43** 1396
- [8] Inagaki S, Tokuzawa T, Itoh K, Ida K, Itoh S I, Tamura N, Sakakibara S, Kasuya N, Fujisawa A, Kubo S *et al.* (LHD Experiment Group) 2011 *Phys. Rev. Lett.* **107**(11) 115001
- [9] Shimozuma T, Kubo S, Idei H, Inagaki S, Tamura N, Tokuzawa T, Morisaki T, Watanabe K, Ida K, Yamada I, Narihara K, Muto S, Yokoyama M, Yoshimura Y, Notake T, Ohkubo K, Seki T, Saito K, Kumazawa R, Mutoh T, Watari T, Komori A and the LHD Experimental Group 2005 *Nucl. Fusion* **45** 1396
- [10] Tamura N, Inagaki S, Tanaka K, Michael C, Tokuzawa T, Shimozuma T, Kubo S, Sakamoto R, Ida K, Itoh K, Kalinina D, Sudo S, Nagayama Y, Kawahata K, Komori A and the LHD experimental group 2007 *Nucl. Fusion* **47** 449
- [11] Moreau D and the TORE SUPRA Team 1992 *Physics of Fluids B* **4** 2165–2175
- [12] Tanaka K, Xiang G, Yin-Xian J, Sakamoto R and Toi K 2004 *Chinese Physics Letters* **21** 2458
- [13] Takenaga H, Nagashima K, Sakasai A, Oikawa T and Fujita T 1998 *Plasma Phys. Control. Fusion* **40** 183
- [14] Tala T, Zastrow K D, Ferreira J, Mantica P, Naulin V, Peeters A G, Tardini G, Brix M, Corrigan G, Giroud C and Strintzi D 2009 *Phys. Rev. Lett.* **102**(7) 075001
- [15] Tardini G, Ferreira J, Mantica P, Peeters A, Tala T, Zastrow K D, Brix M, Giroud C, Pereverzev G V and contributors J 2009 *Nucl. Fusion* **49** 085010
- [16] Mantica P, Tala T, Ferreira J, Peeters A, Salmi A, Strintzi D, Weiland J, Brix M, Giroud C, Corrigan G *et al.* 2010 *Phys. Plasmas* **17** 092505
- [17] Mantica P, Strintzi D, Tala T, Giroud C, Johnson T, Leggate H, Lerche E, Loarer T, Peeters A, Salmi A *et al.* 2009 *Phys. Rev. Lett.* **102** 175002
- [18] Marinoni A, Mantica P, Eester D V, Imbeaux F, Mantsinen M, Hawkes N, Joffrin E, Kiptily V, Pinches S D, Salmi A, Sharapov S, Voitsekovich I, de Vries P, Zastrow K D and contributors J E 2006 *Plasma Phys. Control. Fusion* **48** 1469 URL <http://stacks.iop.org/0741-3335/48/i=10/a=002>
- [19] Zurro B, Hollmann E, Baciero A, Ochando M, Medina F, McCarthy K, Blanco E, de la Cal E, Carralero D, Pedrosa M *et al.* 2011 *Nucl. Fusion* **51** 063015
- [20] Mantica P and Ryter F 2006 *C. R. Phys.* **7** 634–649
- [21] Ryter F, Angioni C, Peeters A G, Leuterer F, Fahrbach H U and Suttrop W (ASDEX Upgrade Team) 2005 *Phys. Rev. Lett.* **95**(8) 085001
- [22] Craig C C 1936 *Ann. Math. Stat.* **7** 1–15
- [23] Hartfuss H J, Giannone L, Stroth U, Erckmann V, Gasparino U, Maassberg H, W7-AS-team and ECRH-team 1994 Heat wave studies on W7-AS stellarator *Proceedings of the workshop on 'Local Transport Studies in Fusion'*, Varenna 1993 pp 119 – 125
- [24] Wambacq P and Sansen W 2013 *Distortion analysis of analog integrated circuits* vol 451 (Springer Science & Business Media)
- [25] Chua L O and Ng C 1979 *Electronic Circuits and Systems, IEE Journal on* **3** 257–269
- [26] Inagaki S, Takenaga H, Ida K, Isayama A, Tamura N, Takizuka T, Shimozuma T, Kamada Y, Kubo S, Miura Y *et al.* 2006 *Nucl. Fusion* **46** 133
- [27] Beyer P, Benkadda S, Garbet X and Diamond P H 2000 *Phys. Rev. Lett.* **85**(23) 4892–4895
- [28] Politzer P A 2000 *Phys. Rev. Lett.* **84**(6) 1192–1195
- [29] Joffrin E, Challis C, Conway G, Garbet X, Gude A, Günter S, Hawkes N, Hender T, Howell D, Huysmans G *et al.* 2003 *Nucl. fusion* **43** 1167
- [30] Inagaki S, Tokuzawa T, Tamura N, Itoh S I, Kobayashi T,

- Ida K, Shimozuma T, Kubo S, Tanaka K, Ido T *et al.* 2013 *Nucl. Fusion* **53** 113006
- [31] Stroth U, Giannone L, Hartfuss H J, ECH Group and the W7-AS Team 1996 *Plasma Phys. Control. Fusion* **38** 611
- [32] Hirsch M, Baldzuhn J, Beidler C, Brakel R, Burhenn R, Dinklage A, Ehmler H, Endler M, Erckmann V, Feng Y, Geiger J, Giannone L, Grieger G, Grigull P, Hartfuss H J, Hartmann D, Jaenicke R, König R, Laqua H P, Maaßberg H, McCormick K, Sardei F, Speth E, Stroth U, Wagner F, Weller A, Werner A, Wobig H, Zoletnik S and for the W7-AS Team 2008 *Plasma Phys. Control. Fusion* **50** 053001 URL <http://stacks.iop.org/0741-3335/50/i=5/a=053001>
- [33] Stroth U 1998 *Plasma Phys. Control. Fusion* **40** 9
- [34] Yamada H, Murakami S, Yamazaki K, Kaneko O, Miyazawa J, Sakamoto R, Watanabe K, Narihara K, Tanaka K, Sakakibara S, Osakabe M, Peterson B, Morita S, Ida K, Inagaki S, Masuzaki S, Morisaki T, Rewoldt G, Sugama H, Nakajima N, Cooper W, Akiyama T, Ashikawa N, Emoto M, Funaba H, Goncharov P, Goto M, Idei H, Ikeda K, Isobe M, Kawahata K, Kawazome H, Khlopenkov K, Kobuchi T, Komori A, Kostrioukov A, Kubo S, Kumazawa R, Liang Y, Minami T, Muto S, Mutoh T, Nagayama Y, Nakamura Y, Nakanishi H, Narushima Y, Nishimura K, Noda N, Notake T, Nozato H, Ohdachi S, Ohyabu N, Oka Y, Ozaki T, Sagara A, Saida T, Saito K, Sasao M, Sato K, Sato M, Seki T, Shimozuma T, Shoji M, Suzuki H, Takeiri Y, Takeuchi N, Tamura N, Toi K, Tokuzawa T, Torii Y, Tsumori K, Watanabe T, Watari T, Xu Y, Yamada I, Yamamoto S, Yamamoto T, Yokoyama M, Yoshimura Y, Yoshinuma M, Mito T, Itoh K, Ohkubo K, Ohtake I, Satow T, Sudo S, Uda T, Matsuoka K and Motojima O 2003 *Nucl. Fusion* **43** 749
- [35] Hartfuss H J, Endler M, Erckmann V, Gasparino U, Giannone L, Grigull P, Herre G, Kick M, Kuhner G, Niedermeyer H, Ringler H, Sardei F, Stroth U, Sattler S, Wagner F and Weller A 1994 *Plasma Phys. Control. Fusion* **36** B17 URL <http://stacks.iop.org/0741-3335/36/i=12B/a=002>
- [36] Diamond P H, Rosenbluth M N, Sanchez E, Hidalgo C, Van Milligen B, Estrada T, Brañas B, Hirsch M, Hartfuss H J and Carreras B A 2000 *Phys. Rev. Lett.* **84**(21) 4842–4845 URL <http://link.aps.org/doi/10.1103/PhysRevLett.84.4842>
- [37] Hilliard J K 1941 *Proceedings of the IRE* **29** 614–620
- [38] Pintelon R, Schoukens J, Vandersteen G and Barbé K 2010 *Mech. Syst. Signal Pr.* **24** 573–595
- [39] Moret J M, Wit T, Joye B and Lister J B 1993 *Nucl. Fusion* **33** 1185–1200
- [40] Khalil H K 1996 *Nonlinear Systems* (Prentice-Hall (NJ))
- [41] Németh J G, Kollár I and Schoukens J 2002 *Instrumentation and Measurement, IEEE Transactions on* **51** 770–775
- [42] Schetzen M 1980 *The Volterra and Wiener Theories of Nonlinear Systems* (Wiley (NY))
- [43] van Berkel M, Zwart H J, Tamura N, Hogeweyj G M D, Inagaki S, de Baar M R and Ida K 2014 *Phys. Plasmas* **21** 112507
- [44] Pintelon R and Schoukens J 2012 *System Identification: A Frequency Domain Approach* (John Wiley and Sons, Hoboken (NJ))
- [45] Iiyoshi A, Komori A, Ejiri A, Emoto M, Funaba H, Goto M, Ida K, Idei H, Inagaki S, Kado S *et al.* 1999 *Nucl. Fusion* **39** 1245
- [46] Suzuki C *et al.* 2012 *Plasma Phys. Contr. F.* **55** 014016
- [47] Takahashi H *et al.* 2014 *Phys. Plasmas* **21** 061506
- [48] Kawahata K, Nagayama Y, Inagaki S and Ito Y 2003 *Rev. Sci. Instrum.* **74** 1449–1452
- [49] Yamada I, Narihara K, Funaba H, Minami T, Hayashi H, Kohmoto T, Group L E *et al.* 2010 *Fusion Sci. Technol.* **58** 345–351
- [50] Lumori M, Geerardyn E, Schoukens J and Lataire J 2014 *IEEE Trans. Instrum. Meas.* **63** 214–220
- [51] Sanchez B, Schoukens J, Bragos R and Vandersteen G 2011 *IEEE Transactions on Biomedical Engineering* **58** 3376–3385 ISSN 0018-9294
- [52] van der Maas R, van der Maas A, Dries J and de Jager B 2016 *Control Engineering Practice* **56** 75–85
- [53] Schneidewind U, van Berkel M, Anibas C, Vandersteen G, Schmidt C, Joris I, Seuntjens P, Batelaan O and Zwart H J 2016 *Water Resour. Res.* **52** 6596–6610
- [54] van Berkel M, Vandersteen G *et al.* 2017 *to be submitted as note to Fusion Engineering and Design*
- [55] van Berkel M, Igami H, Vandersteen G, Hogeweyj G, Tanaka K, Tamura N, de Baar M R, Zwart H J, Kubo S, Ito S, Tsuchiya H and the LHD Experiment Group 2017 New evidence and impact of electron transport nonlinearities based on new perturbative inter-modulation analysis *Proceedings of the 44th EPS Conference on Plasma Physics, Belfast, 26-30 June 2017*
- [56] Tanaka K, Michael C A, Vyacheslavov L N, Sanin A L, Kawahata K, Akiyama T, Tokuzawa T and Okajima S 2008 *Rev. Sci. Instrum.* **79** 10E702
- [57] van Berkel M, Zwart H J, Hogeweyj G M D, Vandersteen G, van den Brand H, de Baar M R and the ASDEX Upgrade Team 2014 *Plasma Phys. Control. Fusion* **56** 105004.